Supporting Information

Transient Secondary and Tertiary Structure Formation Kinetics in the Intrinsically Disordered State of α-Synuclein from Atomistic Simulations

Timo Graen[+], Reinhard Klement[+], Asaf Grupi, Elisha Haas, and Helmut Grubmüller*

Methods

The MD simulations were performed using the Gromacs 5.0.6 [1] software and the four force fields listed in TAB S1 to simulate the 140 amino acid aS. First, we performed temperature replica exchange simulations (T-REX) [2–7], in which the initial structures were chosen at random from a pool of donut shaped model structures derived from NMR-PRE measurements by Bertoncini *et al.* [8]. A NaCl buffer of 100 mM was added to the solvated dodecahedral shaped simulation boxes. For the two AMBER force fields, the Joung et al. [9] ion parameters were used. Each replica was coupled to a thermal bath using the v-rescale [10] thermostat. Further, an isotropic Berendsen barostat [11] with compressibility $1.0 \times 10^{13} \, \text{Bar}^{-1}$ with a 1 ps time constant was applied. PME [12] was used to treat electrostatics with a Fourier grid spacing of 0.135 nm and a direct space cutoff of 1.2 nm for Lennard-Jones and Coulomb interactions for the CHARMM22*/TIP4P-D force field. For all other force fields a Fourier grid spacing of 0.12 nm and a direct space cutoff of 1.0 nm was used. The simulation time step was 4 fs using protein bond constraints [13, 14] and water bond constraints [15].
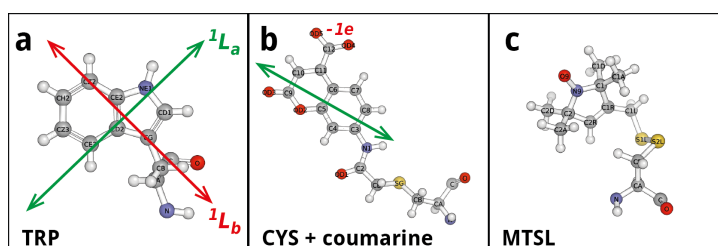

Fig S1. FRET and PRE labels attached to the aS molecules (a) FRET Donor: tryptophan with the two orientations ^1L_a and ^1L_b. (b) FRET Acceptor: cysteine reacted with the probe 7-iodo-acetamidocoumarin-4-carboxylic acid (I-Cou). (c) MTSL nitroxid label for PRE and EPR measurements.

The T-REX system consisted of 40 temperatures covering a range from 295 K to 330 K, see section below. The replicas were equilibrated for 10 ns at their respective temperature before the T-REX swapping was switched on with a swapping attempt frequency of 2 ps. In the T-REX simulations, MTSL labels were mutated at positions 18, 76, 90 and 140, see FIG S1. We

assume here that the MTSL labels do not significantly alter the conformational ensemble of aS, a similar assumption is also made in NMR and EPR experiment. The MTSL label was parametrized for the CHARMM force fields using the parameters of Sezer *et al.* [16], whereas AMBER parameters were derived from Ding *et al.* [17]. We further calculated donor

Table S1. System setups and trajectory lengths for the T-REX simulations, the number of forked FRET simulation trajectories and the total sampling times for the donor fluorescence intensity decay calculations, including all eight FRET label pair positions are shown.

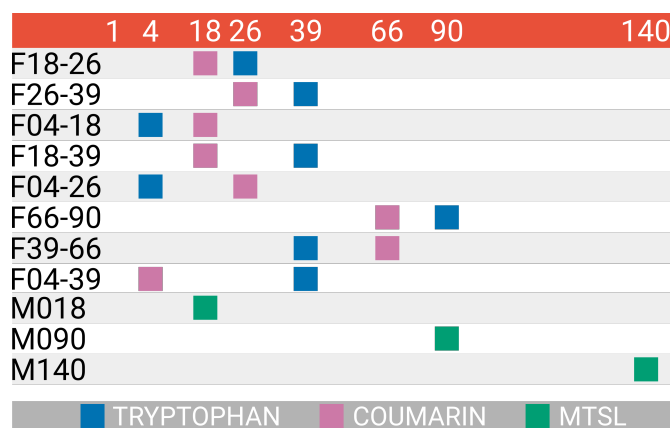| Force Field / Water Model	atoms	box [nm]	T-REX [μs]	#FRET	total [μs]
AMBER03ws [18, 19]/TIP4P2005s [19, 20]	180k	12.0	1.1	1716	65.5
CHARMM22* [21–23] / TIP4P-D [24]	160k	11.8	1.3	1673	66.4
CHARMM22* [21–23] / TIP3P-C [22]	121k	11.8	0.6	1131	54.8
AMBER99sb*ildn [25–27] / TIP3P [28]	138k	12.0	0.6	910	66.7

Fig S2. aS simulation label positions for the eight FRET label pairs of Grupi *et al.* [29, 30] and three MTSL label positions of Schwalbe *et al.* [31]. The top bar (red) depicts the label positions in the sequence and the colored squares indicate the type of label attached as defined in the lower grey bar: FRET donor TRP (blue), FRET acceptor (magenta) and NMR-PRE label MTSL (green).

fluorescence intensity decay trFRET curves from the T-REX generated ensembles. The approximately 5 ns long donor fluorescence decay process cannot directly be extracted from the short ps windows between replica swaps in T-REX simulations. Therefore, an ensemble of 40 ns long trajectories (TAB S1) was forked for each force field and T-REX ensemble. The MTSL labels were removed and the two FRET labels tryptophan (donor) and coumarin (acceptor) (FIG S1) were inserted with random initial orientations at the eight label pair positions (FIG S2). The calculated decay curves include the full chain and label dynamics and all curves were convoluted with the experimental impulse response function.

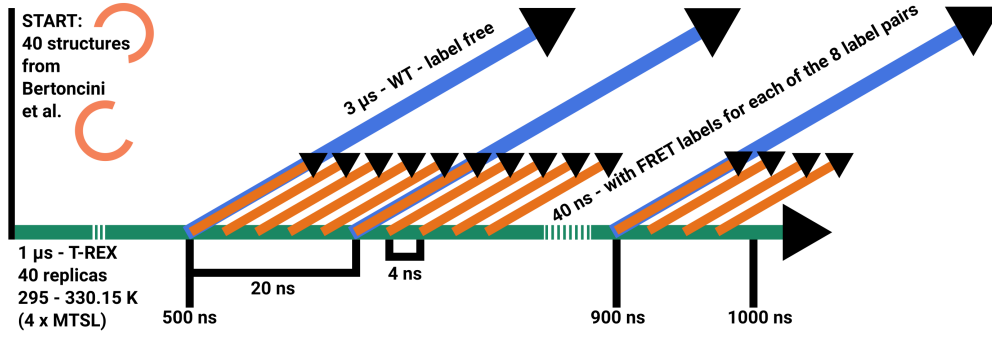In addition to the T-REX and trFRET simulations of the labelled aS, we further simulated

Fig S3. Overview of starting conditions

20 wild type aS trajectories at 300 K, each 3 μs long, using the AMBER03ws/TIP4P2005s force field in a larger simulation box (16.1 nm, 395k atoms) and otherwise unchanged simulation parameters as described for the T-REX simulations. An equilibration time of 1 μs was discarded in the analysis of the time scales for each trajectory.

T-REX temperature ladder

295.00, 295.86, 296.73, 297.59, 298.46, 299.33, 300.20, 301.07, 301.95, 302.83, 303.71, 304.59, 305.48, 306.36, 307.25, 308.13, 309.03, 309.92, 310.82, 311.72, 312.62, 313.52, 314.43, 315.33, 316.24, 317.16, 318.07, 318.98, 319.90, 320.83, 321.75, 322.67, 323.60, 324.53, 325.46, 326.39, 327.33, 328.27, 329.21, 330.15

Trajectory Analysis

The trajectories from the T-REX simulations were Boltzmann re-weighted to a temperature of 300 K using WHAM [32] prior to the analysis. From this re-weighted ensemble, the radii of gyration were calculated for all four force fields using the GROMACS gyrate tool in version 5.0.6 [1]. R_G histograms and 95% confidence intervals were bootstrapped [33] using 10^4 samples with 100 structures per sample. Experimental R_g were calculated from the hydrodynamic radius $R_H = 2.66\ nm$ of Morar et al. [34]. The relation between R_H and R_g of unstructured proteins larger than 50 residues is approximately linearly related $R_g = \varrho R_H$ with $\varrho = 1.06 \pm 0.01$ [35] which yields $R_g(NMR) = 2.8\ nm$. Further, the value $R_g(SAXS) = 3.6\ nm$ [31] was calculated from the raw SAXS profile [36]. SAXS profiles for the MD trajectories were calculated using FOXS v2.1 [37, 38] and 95% confidence intervals were bootstrapped [33] using 10^4 samples with 10 SAXS profiles per sample.

Paramagnetic relaxation enhancement (PRE) profiles were calculated following the Solomon−Bloembergen equations also described in detail by Iwahara [39] and parameters from Esteban et al. [40].

$$\frac{I_0}{I_R} = \frac{R2_{red} \ exp(-\Gamma \tau_{\mathrm{INEPT}})}{R2_{red} + \Gamma}$$ (1)

$$\Gamma = K \ r^{-6} \ \left(4\tau_c + \frac{3\tau_c}{1.0 + \omega_h^2 \tau_c^2}\right)$$ (2)

with $K = 1.23 \ 10^{-8} \, \mathrm{nm}^6/\mathrm{ns}^2$ [40], the proton larmor frequency $\omega_h = 1/23 \, \mathrm{ns}$ [40], the transverse relaxation rate from reduced spectra $R2_{red} = 3.0 \cdot 10^{-9} \, \mathrm{ns}^{-1}$ [40] and the INEPT evolution time being $\tau_{\mathrm{INEPT}} = 10^7 \, \mathrm{ns}$ [40].

The residue specific correlation times τ_c of the electron-nuclear spin interaction vector was calculated from two sets of 20 * 3 μs of WT trajectories for the AMBER03ws/TIP4P2005s and CHARMM22*/TIP4P-D force fields with $\tau_c^{\mathrm{A03WStip4p2005s}} = 6.4 \, \mathrm{ns}$ and $\tau_c^{\mathrm{CS22tip4pD}} = 8.5 \, \mathrm{ns}$. For the TIP3P force fields, only the average tumbling time of the protein from shorter 1 μs of simulation was used $\tau_c^{\mathrm{C22tip3}} = 10.0 \, \mathrm{ns}$, $\tau_c^{\mathrm{A99sb}} = 9.7 \, \mathrm{ns}$. The differences between these two analysis approaches are smaller than the differences due to differences in compactness between the ensembles. The rotational auto correlation time was calculated using the g_rotacf [1] tool for each amino acid using the C-CA-N backbone atoms and subsequently averaged over all amino acids.

The NMR-PRE structur ensemble of Allison et al. [41] was obtained from the Protein Ensemble Database http://pedb.vib.be ID:PED9AAC.

An important source of the intra molecular side-to-side distances within the α-synuclein ensemble are bulk trFRET measurements which depend on the dye-dye orientation factor κ^2 and the reciprocal dye distance R^{-6}. The R^{-6} dependence of the FRET transfer efficiency creates a high sensetivity of trFRET to small changes in distance close to the tryptophan-coumarin Förster radius $R_0 = 2.4 \, \mathrm{nm}$ at which the transfer efficiency is $E_{\mathrm{FRET}} = 0.5$. FRET transfer efficiencies [42, 43], orientation factors, and intensity decay curves [44] can be computed from to the time traces of the fluorescent labels in MD simulations [45]. The time traces of the fluorescent labels further contain die distance information which is challenging to

compute from the experimental fluorescence decay curves alone when κ^2 is not isotropic.

The MD ensembles were compared to the trFRET experiments [29, 30] by calculating time resolved donor fluorescence decay curves [43]

$$I(t) = \left\langle exp\left(-\int_0^t [k_D + k_{ET}(\tau)]d\tau\right)\right\rangle \tag{3}$$

from the forked trajectories with explicit FRET labels present. From the trajectories, the FRET orientation factor

$$\kappa^2(t) = [cos\theta_{DA}(t) - 3cos\theta_D(t)cos\theta_A(t)]^2 \tag{4}$$

was calculated from the angle θ_{DA} between donor and accetor dye, θ_A and θ_D the angles between the dye transition dipole vectors and the distance vector R_{DA} between the two dyes. Both κ^2 and R_{DA} were extracted from the MD trajectories using the g_dyecouple tool [46] in GROMACS 5.1. FRET is based on an ideal dipole-dipole coupling approximation of the radiationless energy transfer process between the donor and acceptor dye for distances between 1-10 nm. In situations were the two dyes are too close to each other, i.e. have Lennard-Jones contacts, the ideal dipole-dipole coupling approximation does no longer hold. Instead, the two dye electron clouds overlap and open a pathway for much faster ps energy transfer mechanisms such as Dexter transfer [47]. In bulk time resolved FRET experiments, these very fast decay processes add an additional fluorescence decay component τ_{Dexter} to the donor fluorescence decay behavior. Depending on the experimental setup [29, 30], the ps time resolution of the photon detector may be larger than time scale of the Dexter process. Thereby, these Dexter configurations are not part of the recorded FRET signal and were also excluded from the FRET analysis of the MD trajectories. Further, all frames were checked for possible contacts with periodic images and periodic frames were removed, the remaining trajectory was split into two independent trajectories for further analysis.

The α-helical and β-sheet frequencies were determined using DSSP [48, 49] for the 20 3 μs long AMBER03ws/TIP4P2005s MD trajectories as well as for the WHAM [32] temperature re-weighted AMBER03ws/TIP4P2005s T-REX ensemble. To account for secondary structure assignment jumps caused by the cut-off criterion in DSSP, the DSSP trajectories were

FRET pair	AMBER99sb*ildn TIP3P	AMBER03ws TIP4P2005s	CHARMM22* TIP3P-C	CHARMM22* TIP4P-D
F18-26	0.70	0.65	0.68	0.65
F26-39	0.62	0.65	0.65	0.64
F04-18	0.67	0.64	0.62	0.65
F18-39	0.66	0.62	0.65	0.66
F04-26	0.57	0.65	0.62	0.64
F66-90	0.66	0.66	0.66	0.64
F39-66	0.68	0.66	0.67	0.67
F04-39	0.66	0.66	0.68	0.67

Table S2. Average orientation factor $\langle \kappa^2 \rangle$ calculated from the short FRET trajectory ensembles.

smoothened using a 15 frame moving average, corresponding to 7.5 ns. We tested window lengths from 1 to 100 frames and observed a plateau in the rates around 7.5 ns in which the rates changed only slowly as a function of the window width. Further, the on-rates and off-rates of α-helical and β-sheet formation and dissociation were determined from a Bayesian estimate [50, 51] of the average rate

$$\langle k \rangle = \frac{\int_0^\infty k \; p(n,m|k) \; p(k) \; dk}{\int_0^\infty p(n,m|k) \; p(k) \; dk} = \frac{n}{T}, \tag{5}$$

with $p(n,m|k) = \exp(-kT)(\Delta t \; k)^n$ and a prior distribution of $p(k)=1/k$. Here, n is the number of forward transitions, T is the total time spend in the state and m is the number of non-transition intervals of length Δt. The standard error $\sigma_k = \sqrt{n}/T$ was derived analogously.
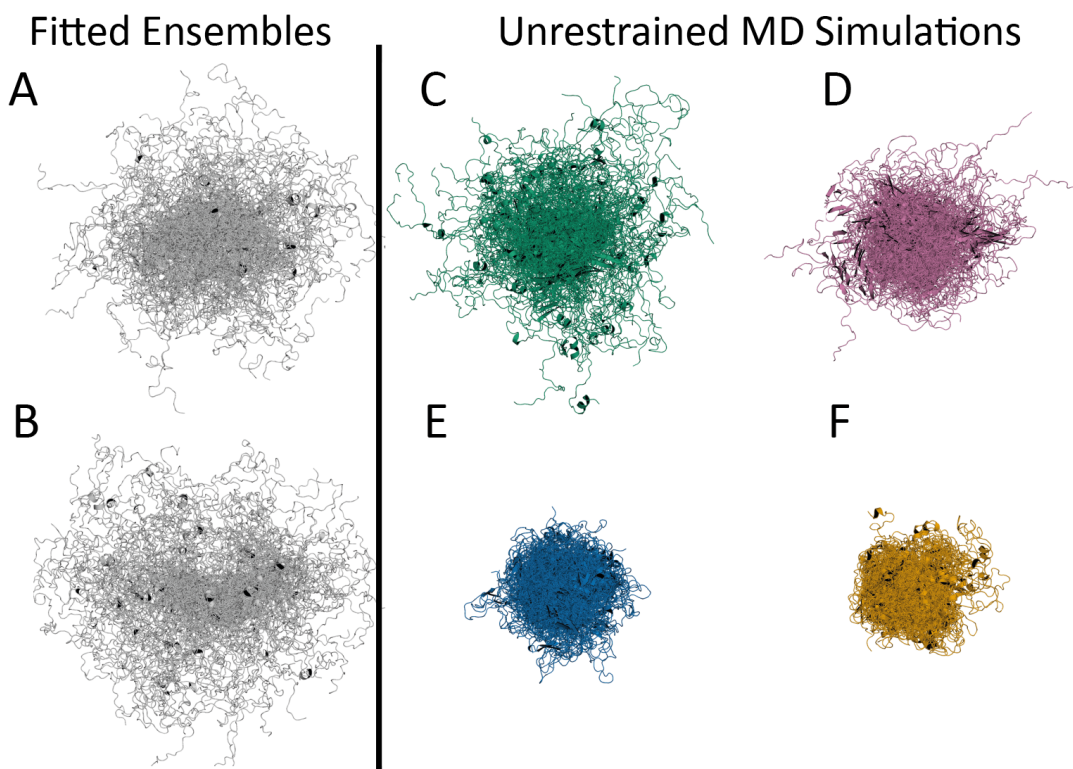
Fig S4. Visual comparison of six aS structural ensembles (left column) Fitted ensembles (A) from NMR-PRE distances by Allison *et al.* [41] and (B) from NMR/SAXS data by Schwalbe *et al.* [31]. This work (center/right column): unrestrained MD simulation ensembles from four different simulation force fields: (C green) AMBER03ws/TIP4P2005s, (D magenta) CHARMM22*/TIP4P-D, (E blue) CHARMM22*/TIP3P-C, (F yellow) AMBER99sb*ildn/TIP3P. Each image consists of 100 snapshots.

Comparison to Fitted Ensembles from Experiment

Figure S4 The AMBER03ws/TIP4P2005s (C green) simulation ensemble agrees best with the fitted models, especially with the NMR-PRE fitted model (A grey). The CHARMM22*/TIP4P-D (D magenta) ensemble yielded the second best agreement. In contrast, the two simulation ensembles FIG S4 E/F, which used the TIP3P-C (E blue) and TIP3P (F yellow) water models, yielded too compact ensembles.

The overall extent of the ensembles converged within the first 100 ns of replica exchange simulations (FIG S5) for all four force fields. The replica exchanges covered the entire replica space with exchange probabilities of $p_{a03ws} = 0.24$, $p_{c22tip4} = 0.23$, $p_{a99sb} = 0.27$ and $p_{c22tip3} = 0.26$.
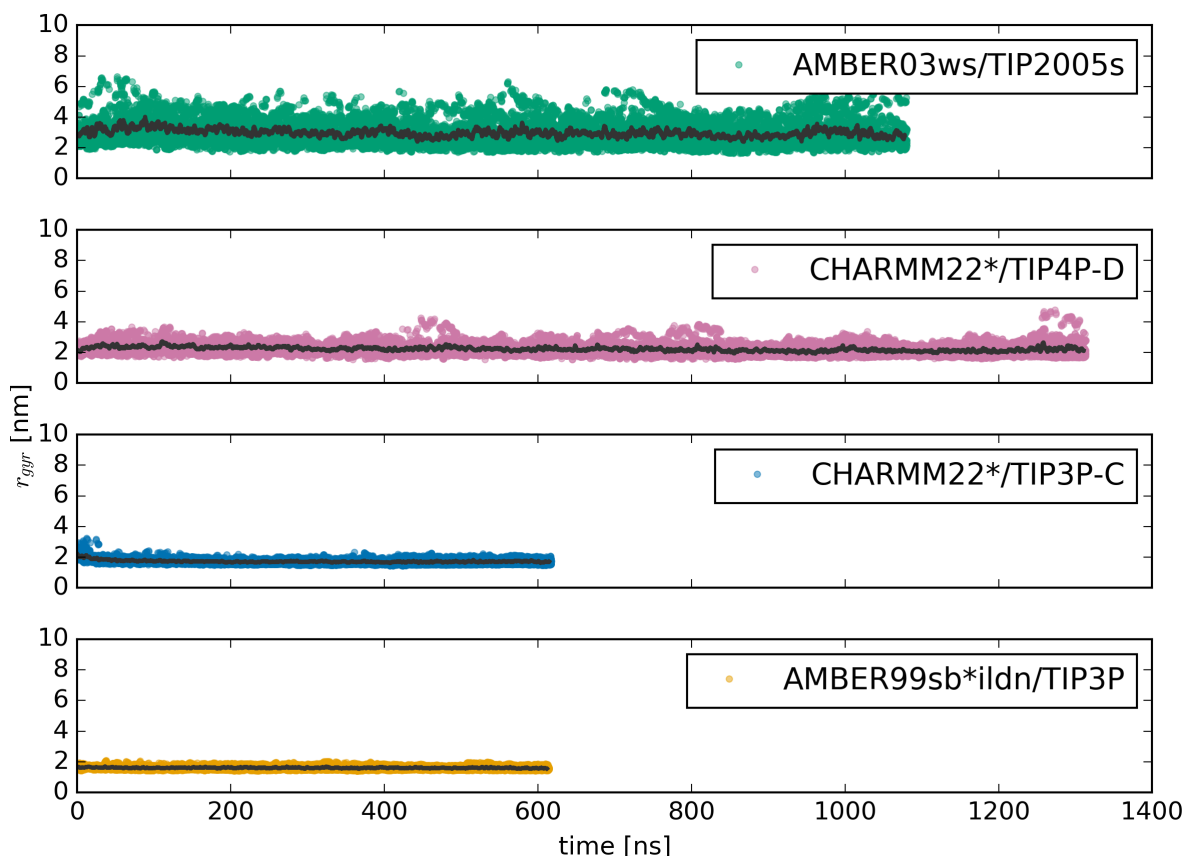
Fig S5. convergence check: Time dependent α-synuclein Radii of Gyration from the T-REX simulations. The grey lines are moving averages with a window size of 50 frames.

Radii of Gyration

Because the radii of gyration FIG S6A provide only one limited and rather global experimental information, which in addition involves an interpretation step on the experimental side, we will subsequently calculate and compare raw data. Specifically, we will focus on SAXS and NMR-PRE profiles, which provide more local and also complementary structural information.

SAXS Profiles

FIG S6B compares experimental [31] with calculated SAXS profiles. All profiles were calculated with the program CRYSOL [52]. Again, the most extended AMBER03ws/TIP4P2005s (green) ensemble agrees best with the raw data and follows the line shape closer than the previous AMBER12/TIP4P-D (not shown) ensemble of Piana *et al.* [24] especially in the small to medium angle range. The second best force field ensemble is CHARMM22*/TIP4P-D (magenta), which largely follows the line shape of the TIP3P (blue/yellow) ensembles while
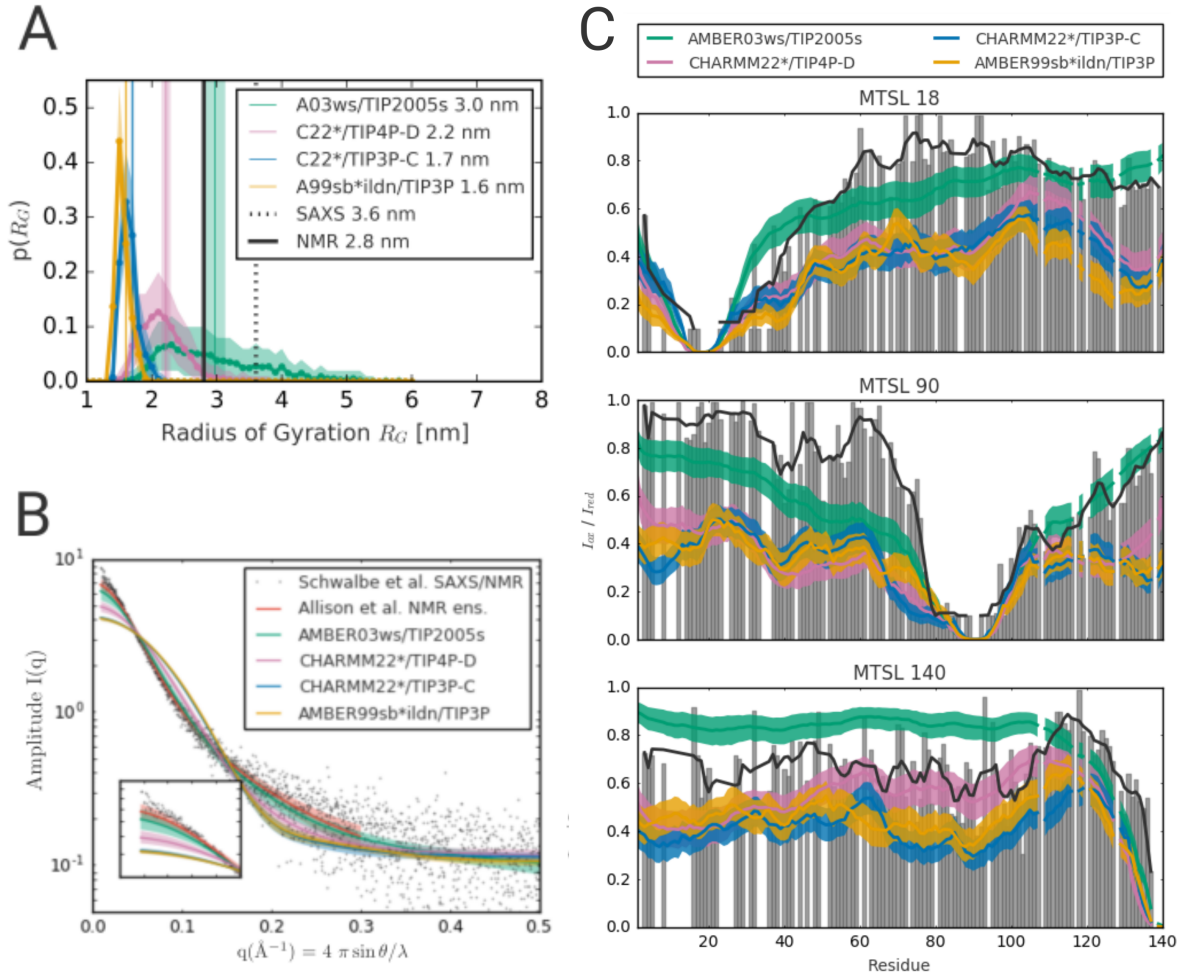
Fig S6. Comparison to experiment: **A** Radii of gyration histograms from replica exchange simulations after WHAM temperature reweighting to 300K. Averages are shown as colored vertical lines with their statistical uncertainty at 2 σ indicated by shaded regions. Experimental references are shown at 3.6 nm and 2.8 nm. **B** Calculated SAXS curves from replica exchange simulations after WHAM temperature reweighting to 300 K. Inset depicts a magnification of the low angle region. **C** Calculated NMR-PRE profiles from replica exchange simulations for MTSL label positions M18, M90 and M140 after WHAM temperature reweighting to 300 K. Experimental values [31] (grey sticks) and their moving average (black line) and standard deviation from differences between neighboring residues (shaded grey).

being slightly more extended in the low angle region. The two TIP3P force fields did not yield

a good agreement with experiment.

We further calculated SAXS profiles for the structural ensemble of Allison *et al.* [41] (see Fig

S7, red line). The resulting SAXS profile has a lower amplitude in the small angle region than

the measured SAXS profile and agrees within error bars with that of the

AMBER03ws/TIP4P2005s (green) ensemble. The agreement of the AMBER03ws/TIP4P2005s

(green) force field with the NMR ensemble [41] (red line) is remarkable as the simulations were

started from independent and more compact starting structures [8]. The remaining discrepancy of both the NMR-PRE ensemble and our AMBER03ws/TIP4P2005s MD T-REX ensemble in the low angle region remains unexplained and might be due to either a sub population of more extended structures not captured by NMR-PRE, or due to a structured water shell that increases the effective radius of gyration in the SAXS experiments [53] or due to remaining force field inaccuracies. Overall, the AMBER03ws/TIP4P2005s (green) ensemble agrees best with the SAXS experiment.
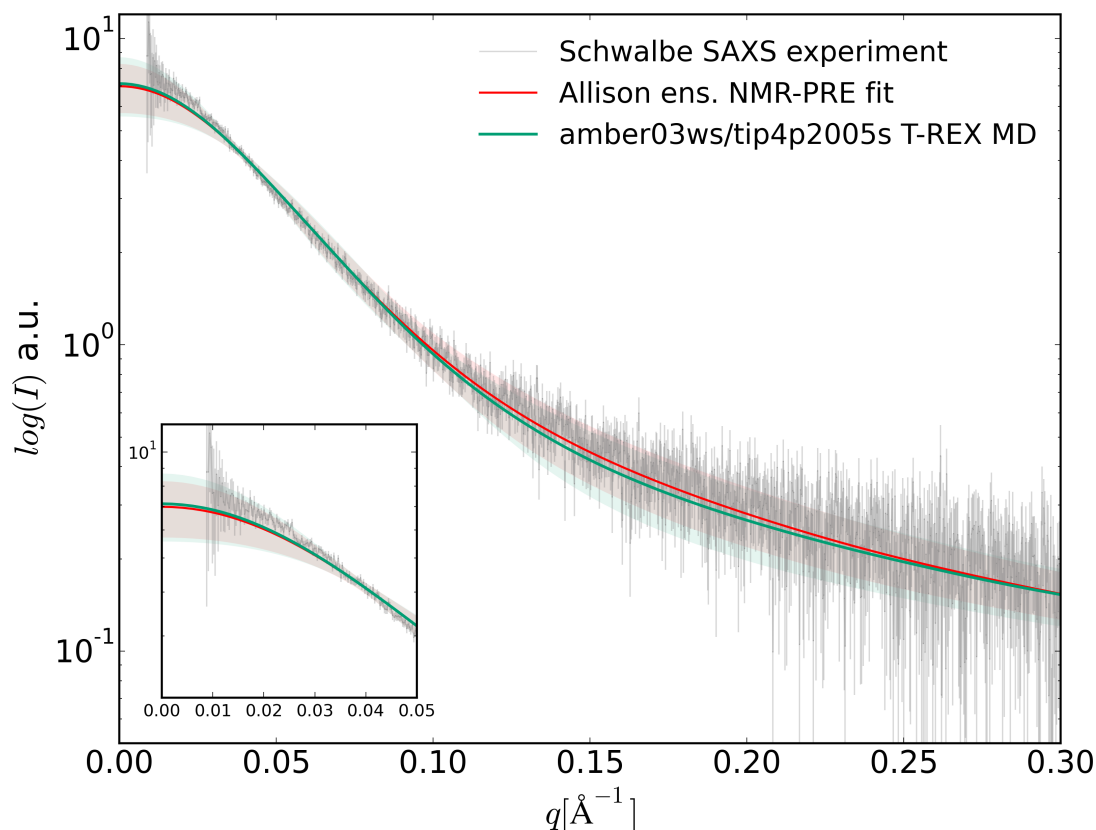
Fig S7. Comparison of calculated SAXS curves from AMBER03ws/TIP4P2005s replica exchange simulations and NMR-PRE model ensemble [41] to experimantal SAXS profile [31]. The inset depicts a magnification of the low angle region.

NMR-PRE Profiles

FIG S6C shows the calculated NMR-PRE profiles from the T-REX ensemble for positions M18, M90 and M140. The best agreement for positions M18 and M90 was found for the AMBER03ws/TIP4P2005s (green) ensemble, whereas the CHARMM22*/TIP4p-D (magenta) force field yields best agreement for the C-terminal interactions at position M140. Again, the largest deviations from experiment were seen for the CHARMM22*/TIP3P-C (blue) and

AMBER99sb*ildn/TIP3P (yellow) force fields. The interactions between the terminal position M140 and the rest of the protein chain was overestimated in AMBER03ws/TIP4P2005s (green), whereas CHARMM22*/TIP4p-D (magenta) overestimated the interaction between the position M18 and M90 with the NAC and C-terminal region. There are deviations in the close vicinity of the MTSL label which may be caused by errors in the estimation of the PRE constants and electron-nuclear interaction vector correlation times. However, the relative scoring of the force fields did not change under variation of the PRE constants, $R2_{\mathrm{red}}$ and τ_{INEPT}. We did not have access to the experimental data for position 76.

The comparison of the simulated and the measured PRE profiles is complicated by noise as well as by the large number of indirectly measured data points. We therefore also compared the ensembles with independent trFRET donor decay curves and calculated distances as described in the following paragraphs.

Fluorescence Intensity Decay Curves - trFRET

In FIG S8A, time resolved FRET donor fluorescence decay curves are shown for eight label pair positions [29, 30]; FIG S8B shows the respective integrated differences between measured and calculated curves. The AMBER03ws/TIP4P2005s (green) and CHARMM22*/TIP4P-D (magenta) force fields best predicted the experimental decay curves with the exception of the two short distances at label pair positions, F18-26 and F26-39, which were best described in the more compact CHARMM22*/TIP3P-C (blue) ensemble.

Because the direct comparison of the calculated decay curves rests on the assumption that the decay characteristics of tryptophan in our simulations are sufficiently well described by a single exponential decay with only one averaged donor decay life time, we further compared the distances from the MD simulations to the distances derived from experiment, see FIG S9. The distances observed in the AMBER03ws/TIP4P2005s ensemble agreed much closer than the CHARMM22*/TIP4P-D and the TIP3P derived distances.

Residue Contact Maps and Residue Correlation Times

The inter residue correlation times $\langle \tau \rangle$ were calculated from mono-exponential fits to the auto correlation curves between all Cα atoms with a lag time of 1000ns. Correlation time maps were
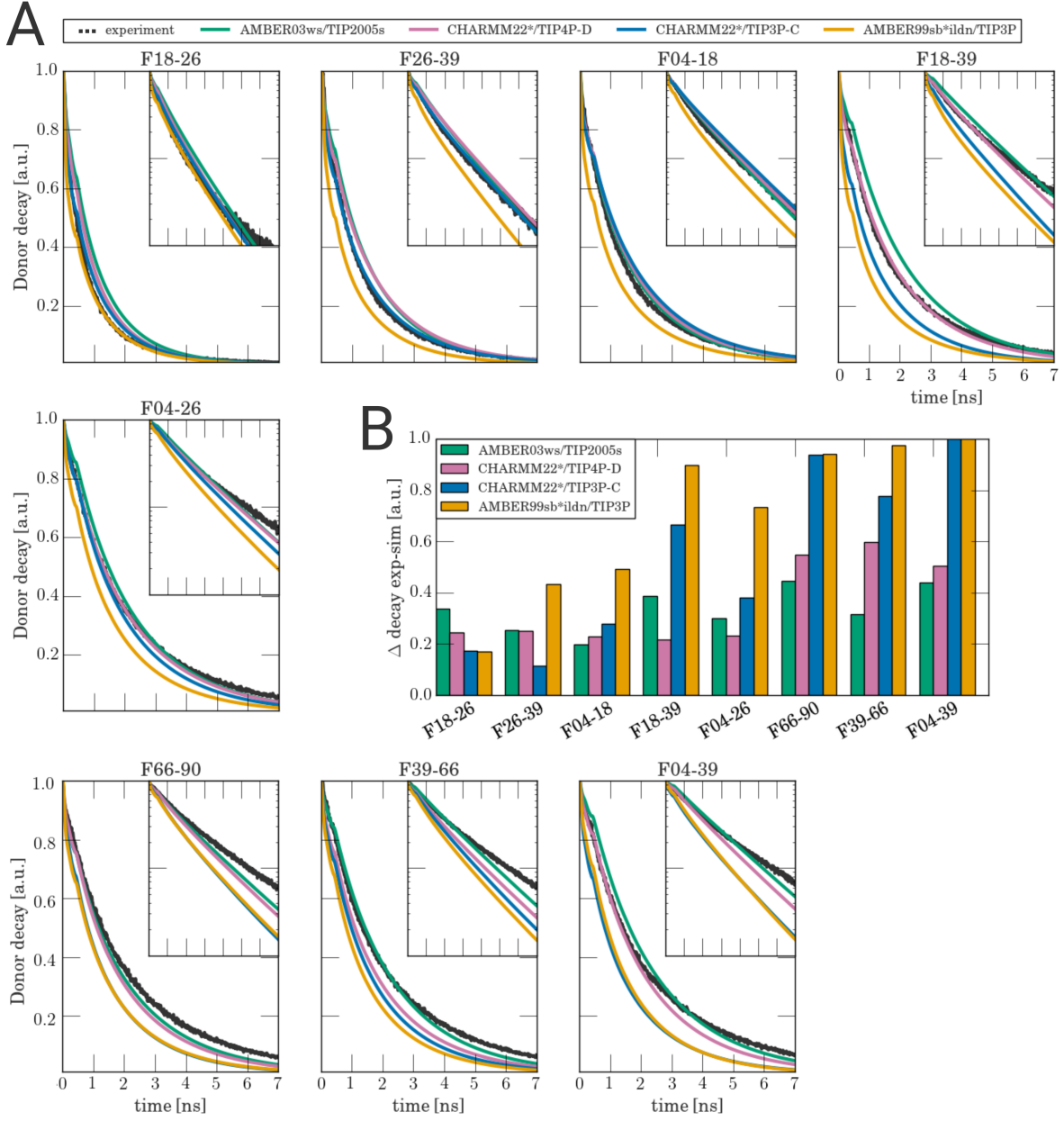
Fig S8. Comparison to trFRET experiments: **A** Calculated trFRET donor fluorescence intensity decay curves are shown for all four force fields (colored lines) and eight label pair positions together with the experimental decay curves [29, 30](black dots). Insets depict the same data on a logarithmic scale. **B** Integrated difference between the calculated and experimental donor decay curves.
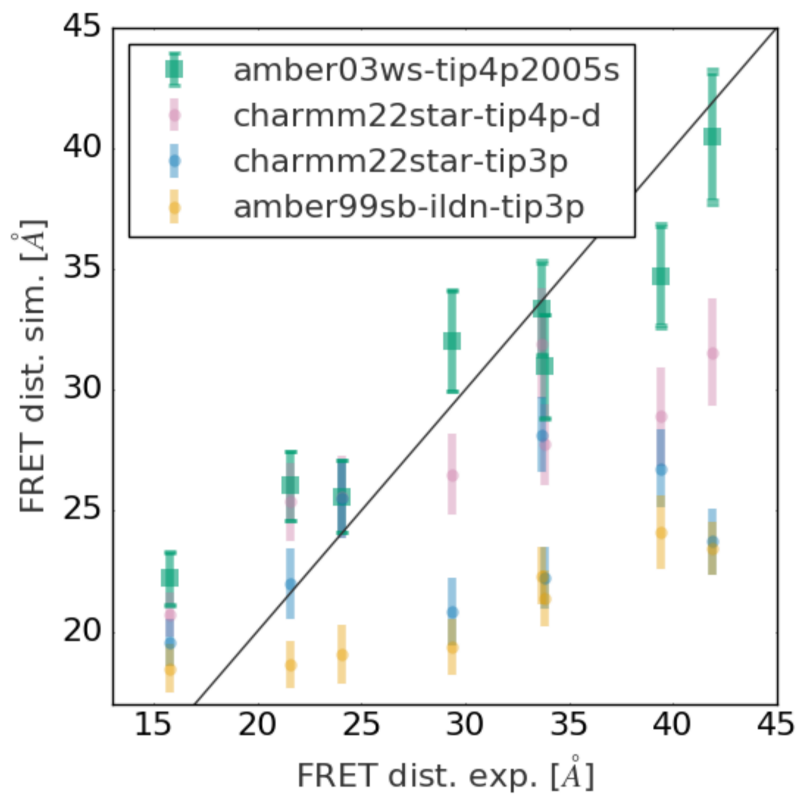
Fig S9. Comparison of MD and trFRET distances: Comparison of the mean dye-dye distances from the four MD ensembles to the mean distances derived from trFRET [29,30].

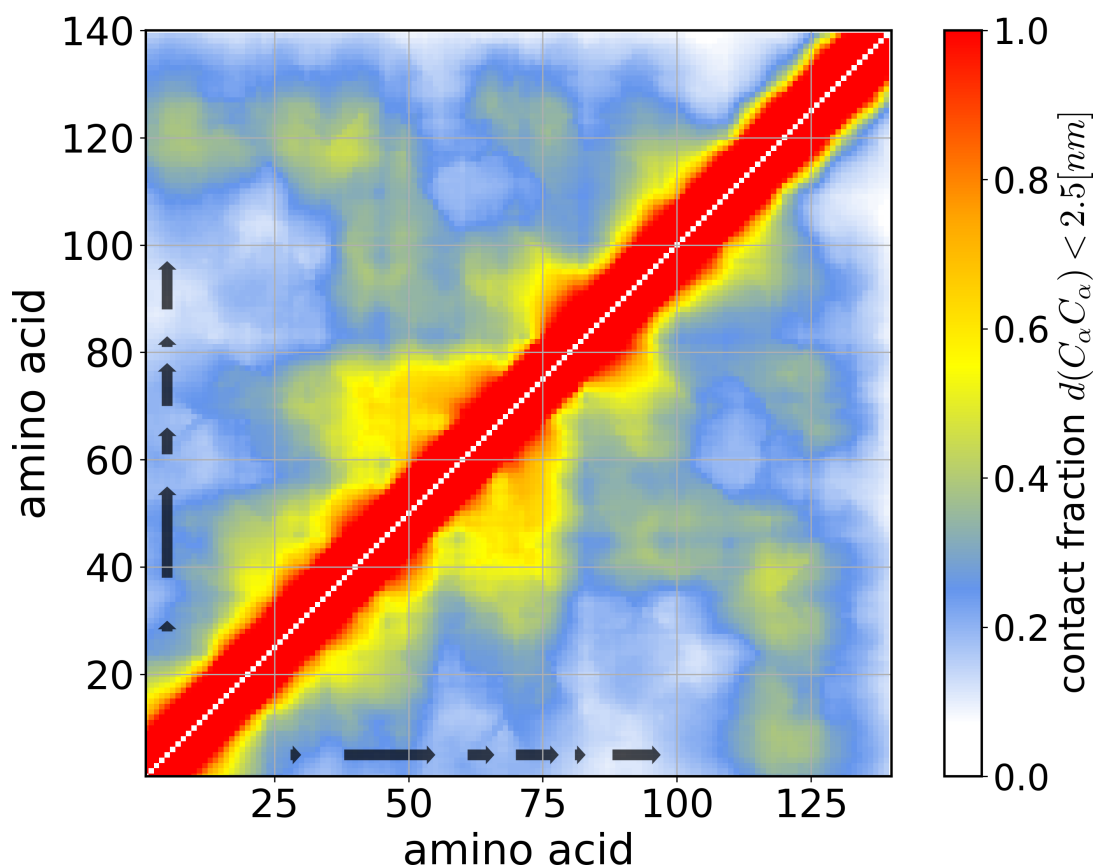averaged over 20×3 μs AMBER03ws/TIP4P2005s force field trajectories.

Fig S10. Amino acid contact fractions for all combinations of residue-residue interactions using a 2.5 nm contact cut-off. The contact fractions were averaged over $20\times3\,\mu$s trajectories from the AMBER03ws/TIP4P2005s force field.
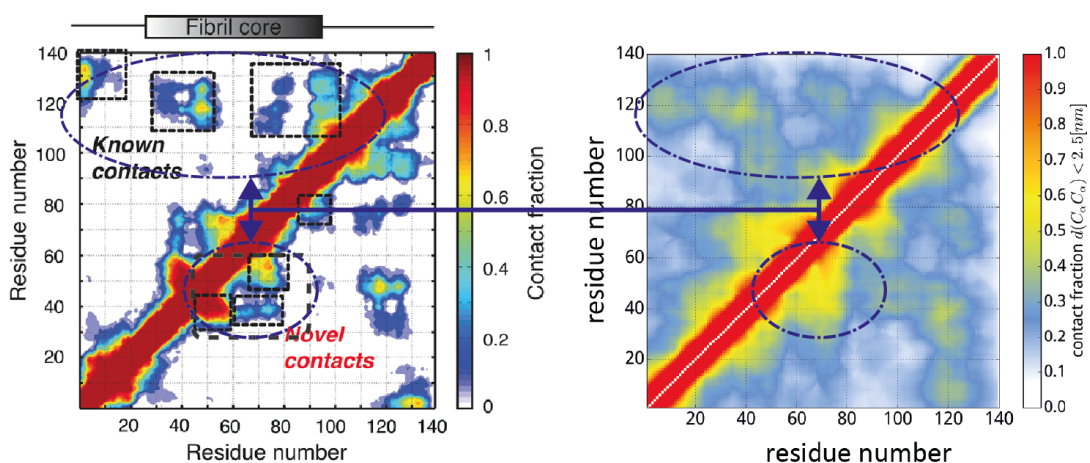

Fig S11. Comparison of the contact fraction maps *left*: calculated from NMR-PRE data by Esteban-Martin et al., BiophysJ 2013 and *right*: from our unrestrained MD simulations.
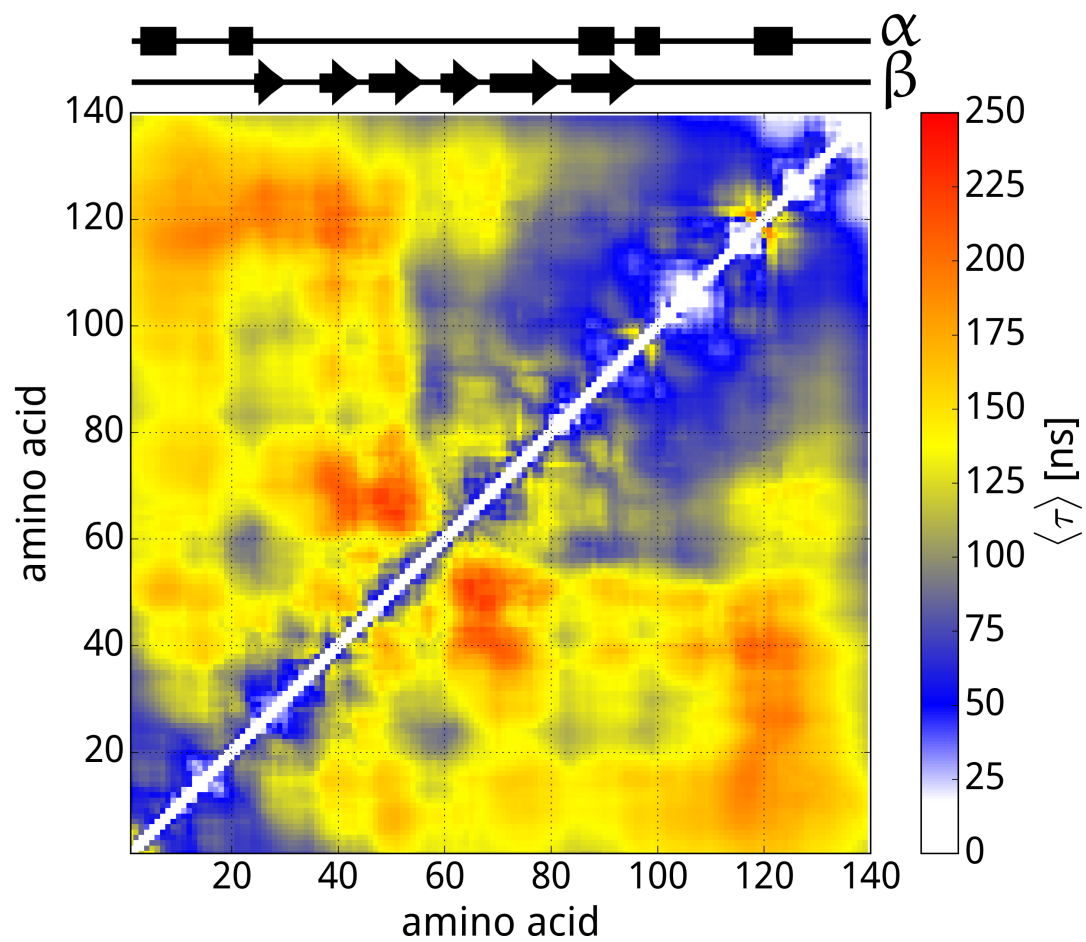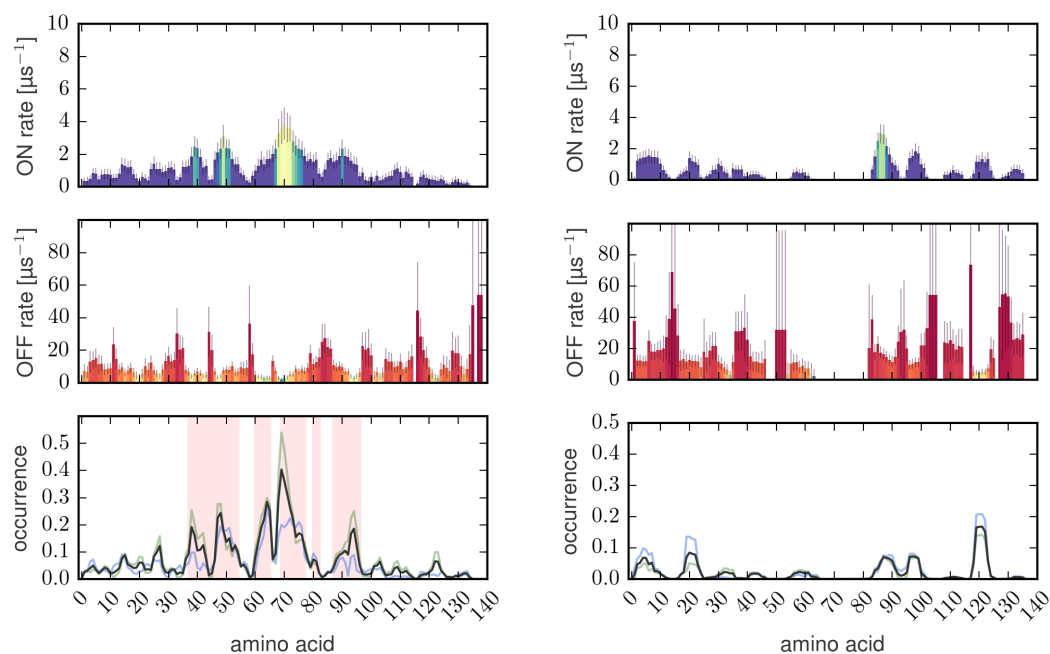
Fig S12. Amino acid correlation times calculated for all Cα distances. Regions of transient structure formation are shown above.

Time Scale Analysis.

(a) β-sheet   **(b)** α-helix

Fig S13. a) β-sheet and b) α-helix formation (top) and dissociation (center) timescales with error bars at 2σ. Relative occurrence of the secondary structure content (bottom) for T-REX trajectories (blue), long WT trajectories (red) and weighted with a 40/60 ratio (black). (AMBER03WS)

Details about the α-helix formation and dissociation rates are shown in FIG S13. The formation rates were again consistently slower than the dissociation rates. As a result, the population of α-helices is markedly smaller compared to the β-sheets with only one peak at residue 122, exhibiting occurrences over 10%. The helix forming residues [54] in the amino acid range of 1-100 show the largest helical content at the beginning (residues 1-10, 20-25) and at the end (residues 85-91, 93-100) of the range. The membrane induced formation of α-helical structures may depend on a partial stabilization of these high propensity regions with fast k_{on} rates first. The peak at residues 119-124 further suggests at least a partial stabilization of the otherwise unstructured C-terminus as well.

The peaks for α-helix and β-sheet rates are shown in TAB S3.

We further checked the convergence of the rate estimates between the first and the second half of the trajectories used in the analysis (FIG S14, FIG S15) and did not observe larger differences in the predicted rates outside the shown error margins in the main text. The β-sheet

(a) β-sheet
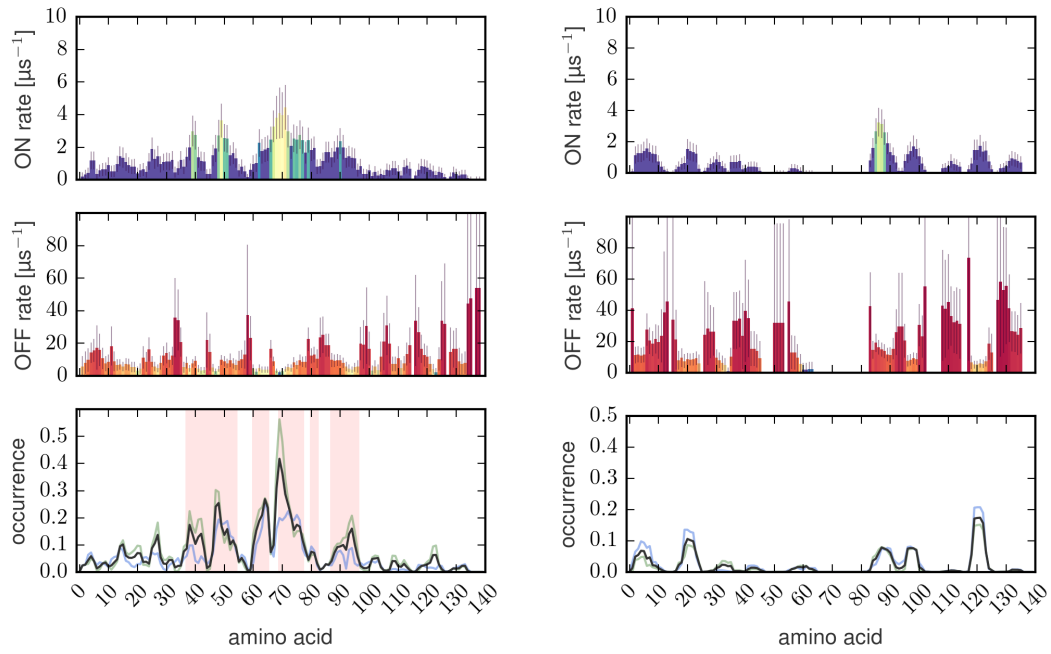
(b) α-helix

Fig S14. Same as FIG S13 but only using data from μs 1-2 from 20 trajectories

(a) β-sheet
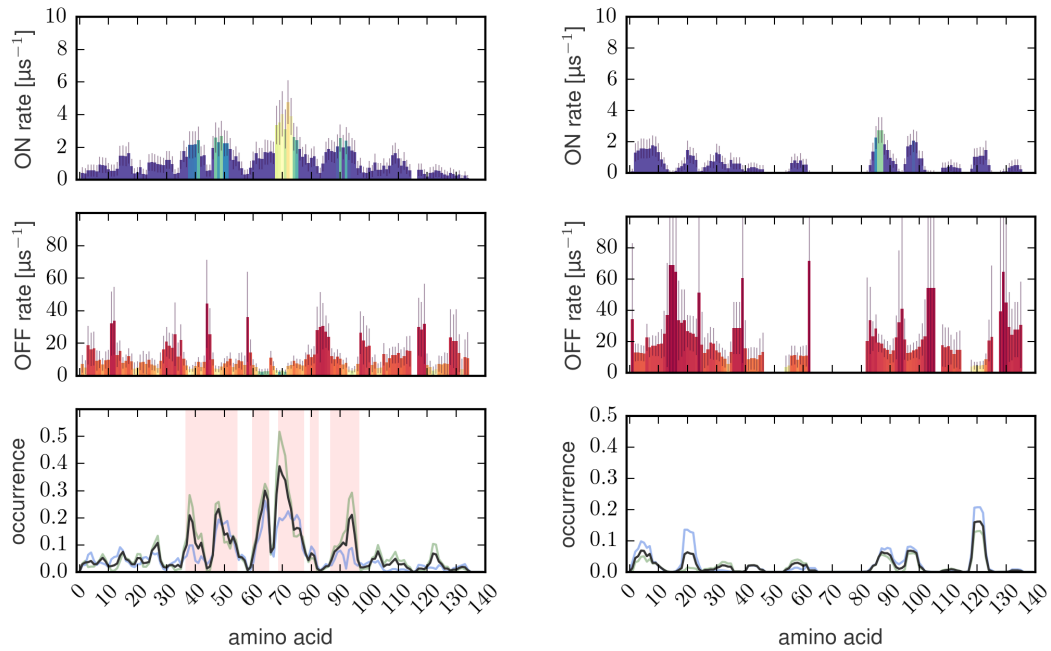
(b) α-helix

Fig S15. Same as FIG S13 but only using data from μs 2-3 from 20 trajectories

Table S3. Peaks of secondary structure formation and dissociation rates for β-sheets (top) and rates for α-helices (bottom) are shown together with the relative occurrence in long trajectories and from T-REX sampling.

peak	$k_{on}^{\beta} \pm 2\sigma$ [µs^{-1}]	$k_{off}^{\beta} \pm 2\sigma$ [µs^{-1}]	occurrence [%]
39	1.8 ± 0.9	3.9 ± 2.0	18
48	2.2 ± 1.1	3.6 ± 1.8	22
65	1.2 ± 0.8	2.3 ± 1.5	29
70	4.5 ± 1.9	2.9 ± 1.2	38
95	2.8 ± 1.2	3.5 ± 1.7	22

peak	$k_{on}^{\alpha} \pm 2\sigma$ [µs^{-1}]	$k_{off}^{\alpha} \pm 2\sigma$ [µs^{-1}]	occurrence [%]
6	1.6 ± 0.8	10 ± 5	8
21	1.2 ± 0.6	36 ± 20	6
59	0.8 ± 0.5	7.9 ± 5.2	4
88	3.4 ± 1.2	16 ± 5	8
98	2.2 ± 0.9	12 ± 5	8
122	1.3 ± 0.7	6.1 ± 3.4	14

occurrences at positions 39, 70 and 95 were slightly smaller in the MTSL labelled T-REX ensemble than for the WT ensemble derived from the long trajectories. We think the differences are either due to very slow processes with timescales larger than several µs or due to perturbations introduced by the relatively small MTSL labels.

Length distribution of residues in secondary structure elements

Secondary structure content was calculated with the program DSSP [48, 49]. Structured elements mostly occur only over short stretches of 2-3 (β-sheets) or 4-5 (α-helices) aminoacids. The overall content of 2% α-helices and 7.5% β-sheets is in good agreement with values obtained from CD/FTIR measurements [55, 56].
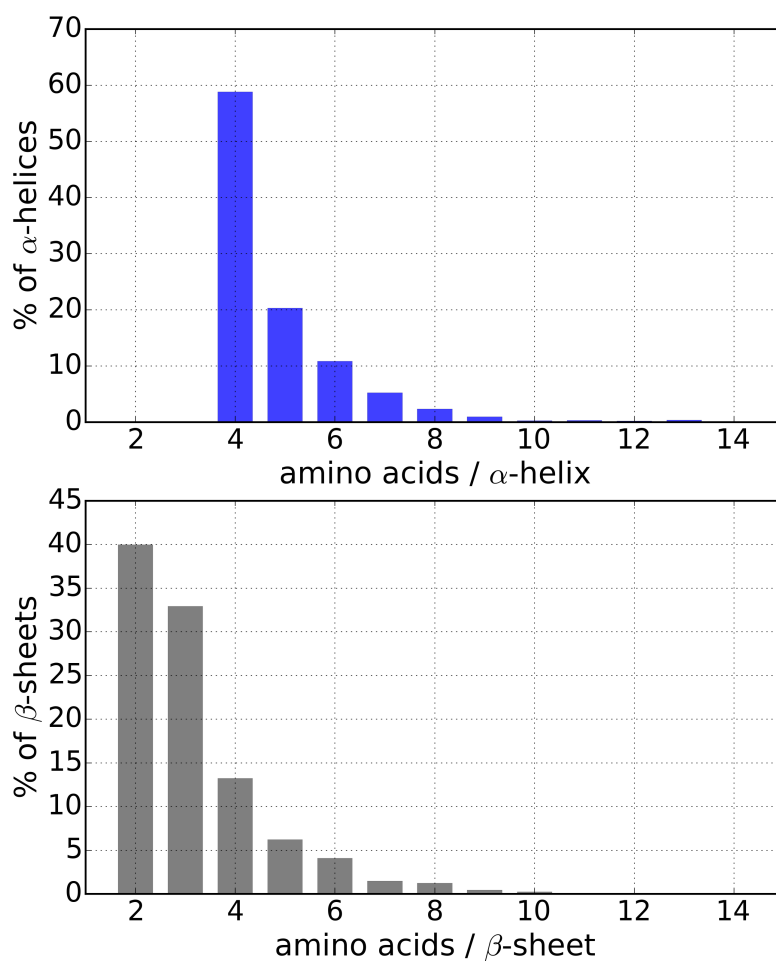

Fig S16. Amino acid length distribution of α-helices and β-sheets in the amber03ws long trajectories.

Comparison to experimental J-couplings

J-couplings for all four force fields were calculated from the REX-ensemble at $300.2\,\mathrm{K}$ and compared to experimental data from Mantsyzov et al. [57]. 95% confidence intervals were bootstrapped [33] using 10^4 samples with 10 profiles per sample.

J-coupling	Karplus Relation
$^1J_{C\alpha H\alpha}$	$^1J_{C\alpha H\alpha} =$ [RESIDUE SPECIFIC] $+ 1.4\ sin(\psi + 138°)$ $- 4.1\ cos2(\psi + 138°) + 2.0\ cos2(\phi + 30°)$ *refence: Vuister et al [58]* IDP reference (sec. coupl.): Gapsys et al. [59]
$^1J_{NC\alpha}$	$^1J_{NC\alpha} =$ $8.65 - 1.21\ cos(\psi) + 2.85\ cos^2(\psi)$ *reference: Wirmer et al. [60]*
$^2J_{N(i)C\alpha(i-1)}$	$^2J_{N(i)C\alpha(i-1)} =$ $-1.51\ cos(\psi) - 0.66\ cos^2(\psi) + C$ $C{=}7.65$ *for VAL, ILE, THR and SER;* $C{=}8.14$ *all others* *reference: Mantsyzov et al. [57]*
$^3J_{HNH\alpha}$	$^3J_{HNH\alpha} =$ $7.97\ cos^2(\phi - 60°) - 1.26\ cos(\phi - 60°) + 0.63$ *reference: Vuister et al. [61], Vögeli et al. [62]*

Table S4. Karplus relations used to calculate the ^1J, ^2J and ^3J couplings.

Force Field/Water Model	$^1J_{NC\alpha}$	$^1J_{H\alpha C\alpha}$	$^2J_{N(i)C\alpha(i-1)}$	$^3J_{HNH\alpha}$
AMBER03ws/TIP4P2005s	0.364	0.987	0.324	0.598
CHARMM22*/TIP4P-D	0.263	0.787	0.331	0.588
CHARMM22*/TIP3P-C	0.311	0.724	0.316	0.624
AMBER99sb*ildn/TIP3P	0.391	0.953	0.557	0.599

Table S5. Average Unsigned Error for all four force fields and J-couplings in Hz.
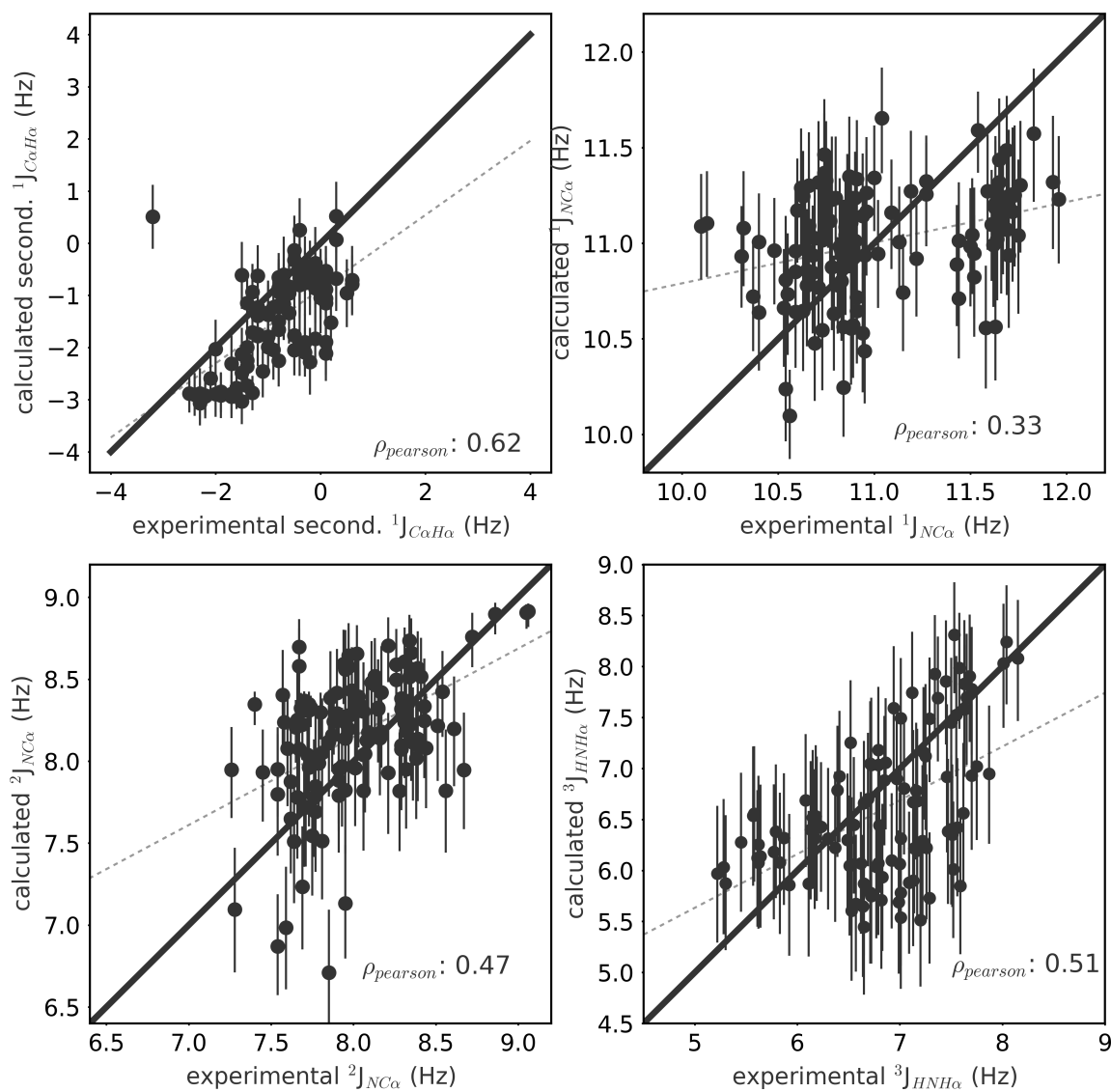
Fig S17. Comparison of calculated J-couplings from our AMBER03ws simulations (y-axis) and the NMR experiments (x-axis) [57]. Secondary $^1J_{C\alpha H\alpha}$ couplings were calculated using the reference IDP values of Gapsys et al. [59].
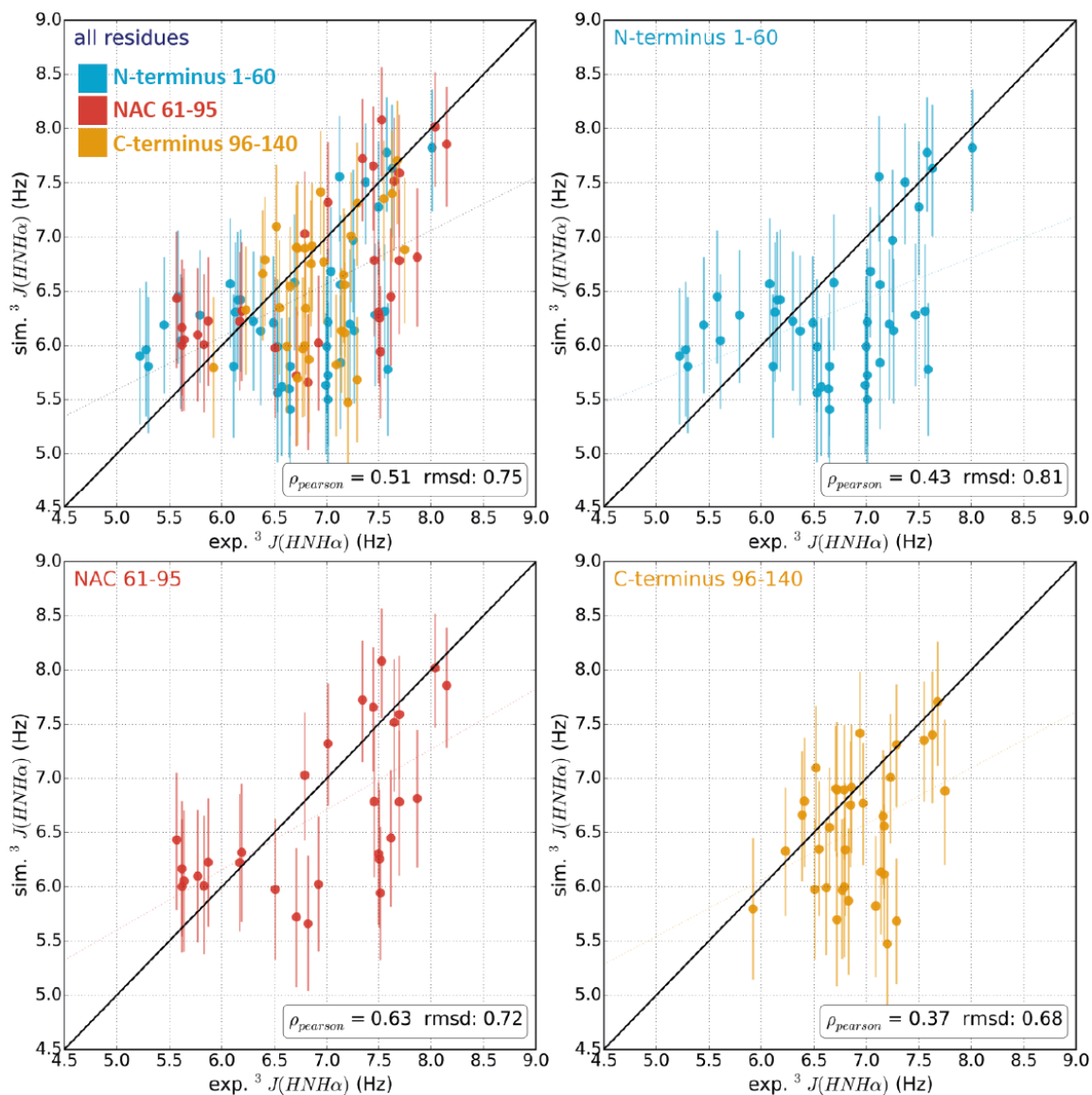
Fig S18. Comparison of the contribution of calculated $^3J_{HNH\alpha}$ coupling from our AMBER03ws simulations with respect to aS structural regions and NMR experimental data [57].
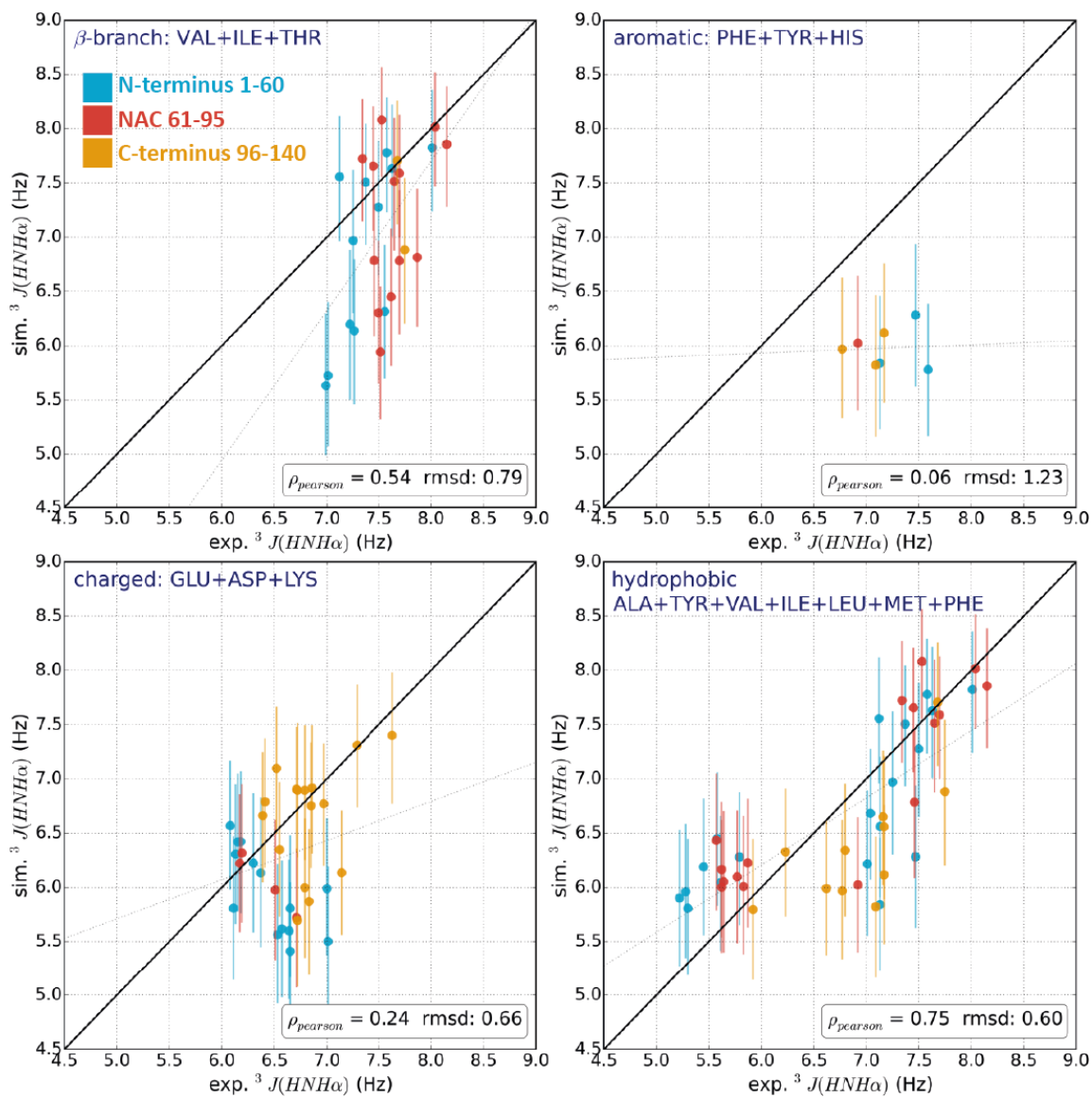
Fig S19. Calculated $^3J_{HNH\alpha}$ coupling from our AMBER03ws simulations for functional sets of amino acid groups.
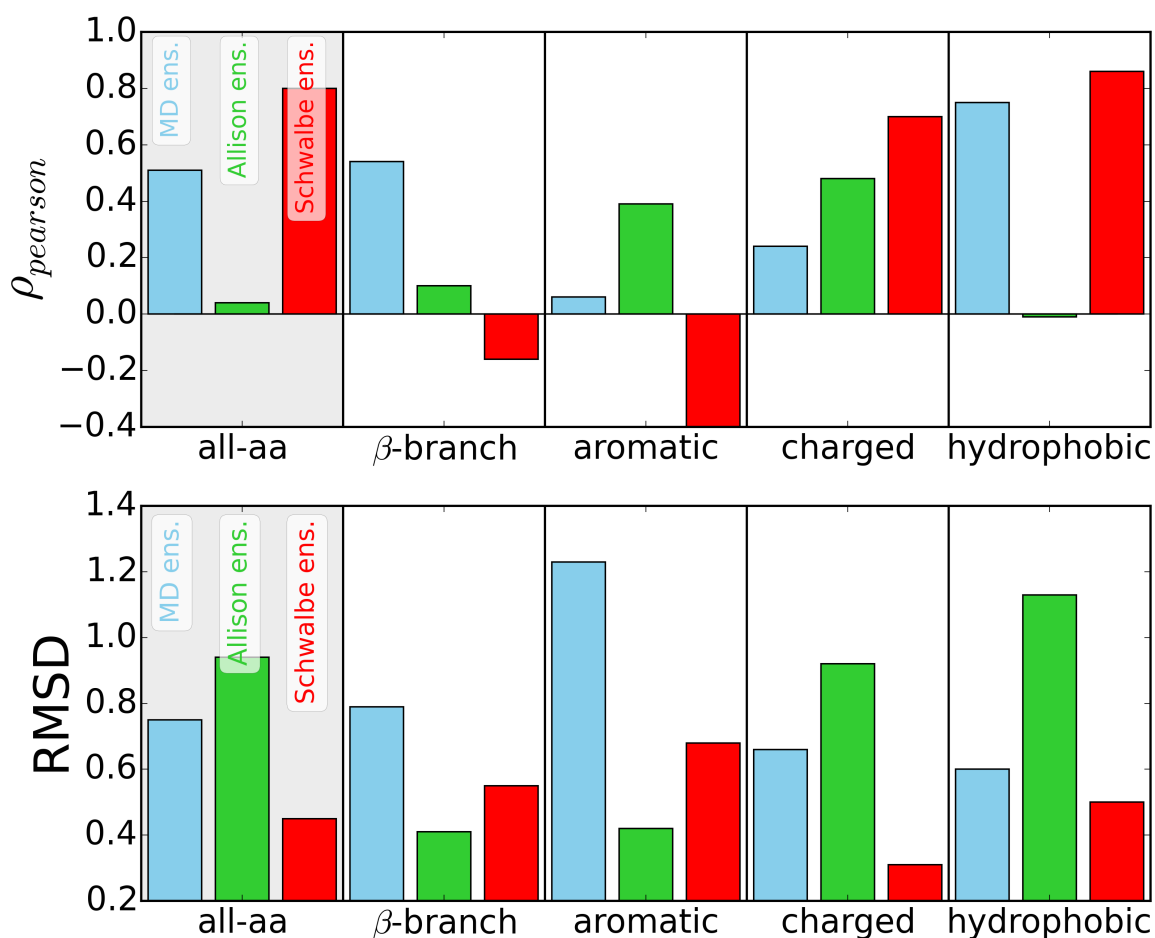
Fig S20. Correlation comparison of $^3J_{HNH\alpha}$ couplings calculated from our AMBER03ws ensemble, the NMR-PRE model ensemble of Allison et al. [41] and the NMR-PRE, SAXS, chemical shift and J-coupling model ensemble of Schwalbe et al. [31] with respect to experimental data from Mantsyzov et al. [57] . β-branch: VAL, ILE, THR. Aromatic: PHE, TYR, HIS. Charged: GLU, ASP, LYS. Hydrophobic: ALA, TYR, VAL, ILE, LEU, MET, PHE.
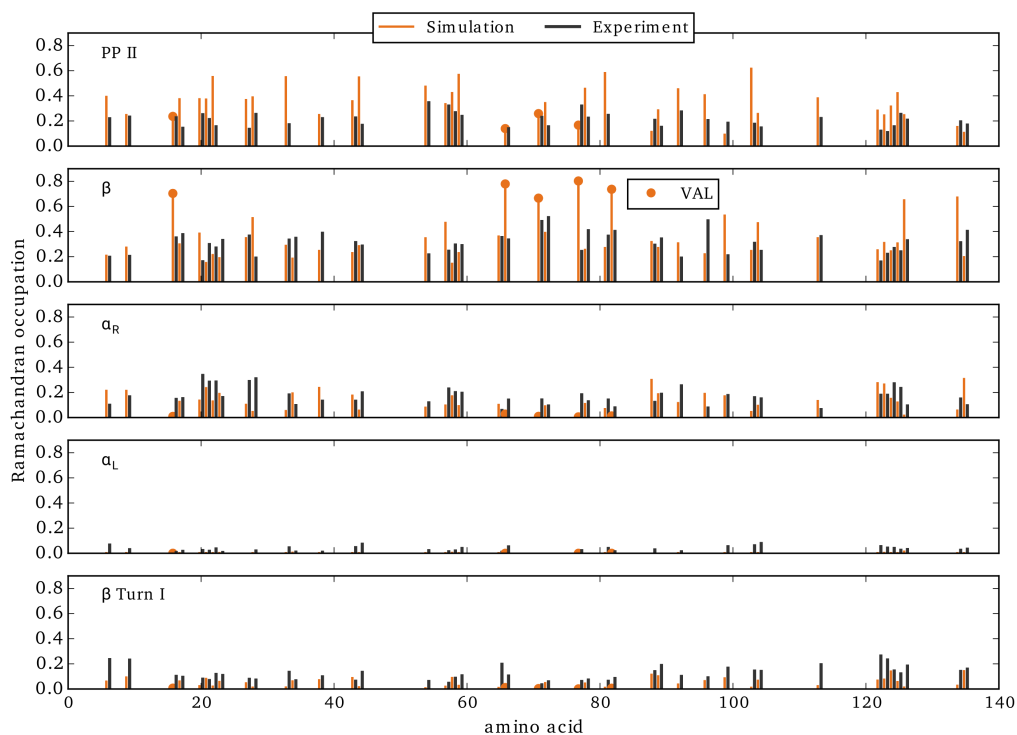
Fig S21. Comparison of experimental Ramachandran occupations [57] (black bars) to calculated occupations (orange bars) from the AMBER03 trajectories using the same segmentation as described by Mantsyzov et al. [57]. Again, a 40/60 ratio was used, as described in Figure 1 main text, between the WHAM re-weighted T-REX trajectories and long WT trajectories. Valine residues are highlighted (orange points) to illustrate residue specific deviations in β-sheet Ramachandran occupations.

We calculated spectral densities [63] from our unrestrained MD ensemble for all structures, each frame separated by 100ps. This was done without fitting the structures to an initial frame of reference. The comparison of back calculated spectral densities with the the experimental data shows a slowed down motion in the core region of aS with peaks at the positions of the valine residues. The VAL residues are those which show the largest deviation in the Ramachandran occupancies derived from the same NMR data set [57].
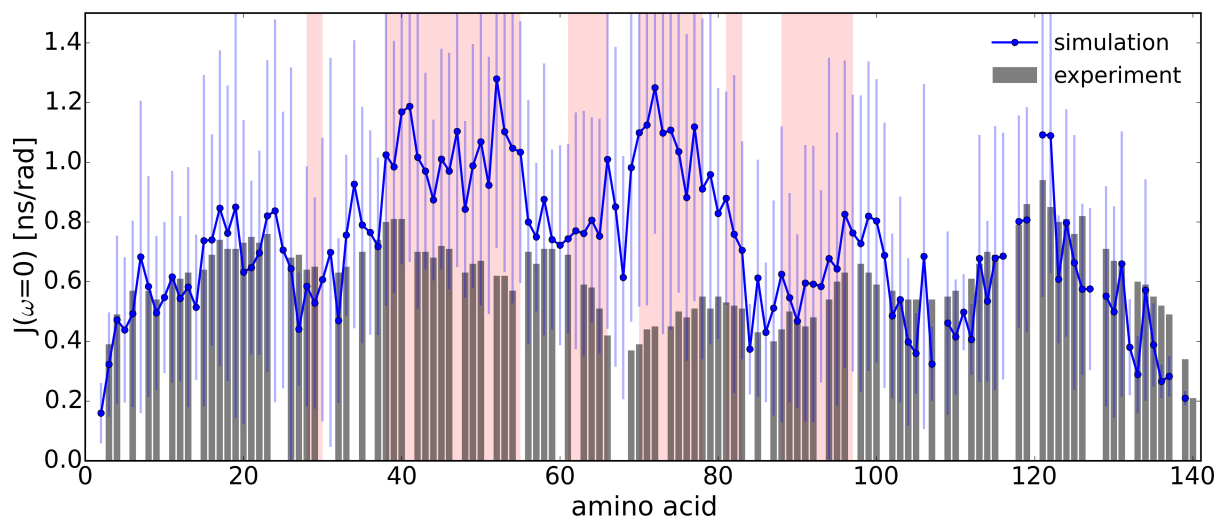
Fig S22. Spectral densities of backbone amide ^{15}N-^{1}H back calculated from simulations compared to experimental values from Mantsyzov et al. Protein Science 2014 [57].

Fig S23. Comparison of exprimental secondary chemical shifts (x-axis) of Mantsyzov et al. [57] and calculated [64] shifts from the AMBER03ws trajectories (y-axis). Random coil reference data at 301 K and pH7 [65,66] was used. N-terminus(blue) res. 1-60, NAC(gray) res. 61-95, C-terminus(orange) res. 96-140.

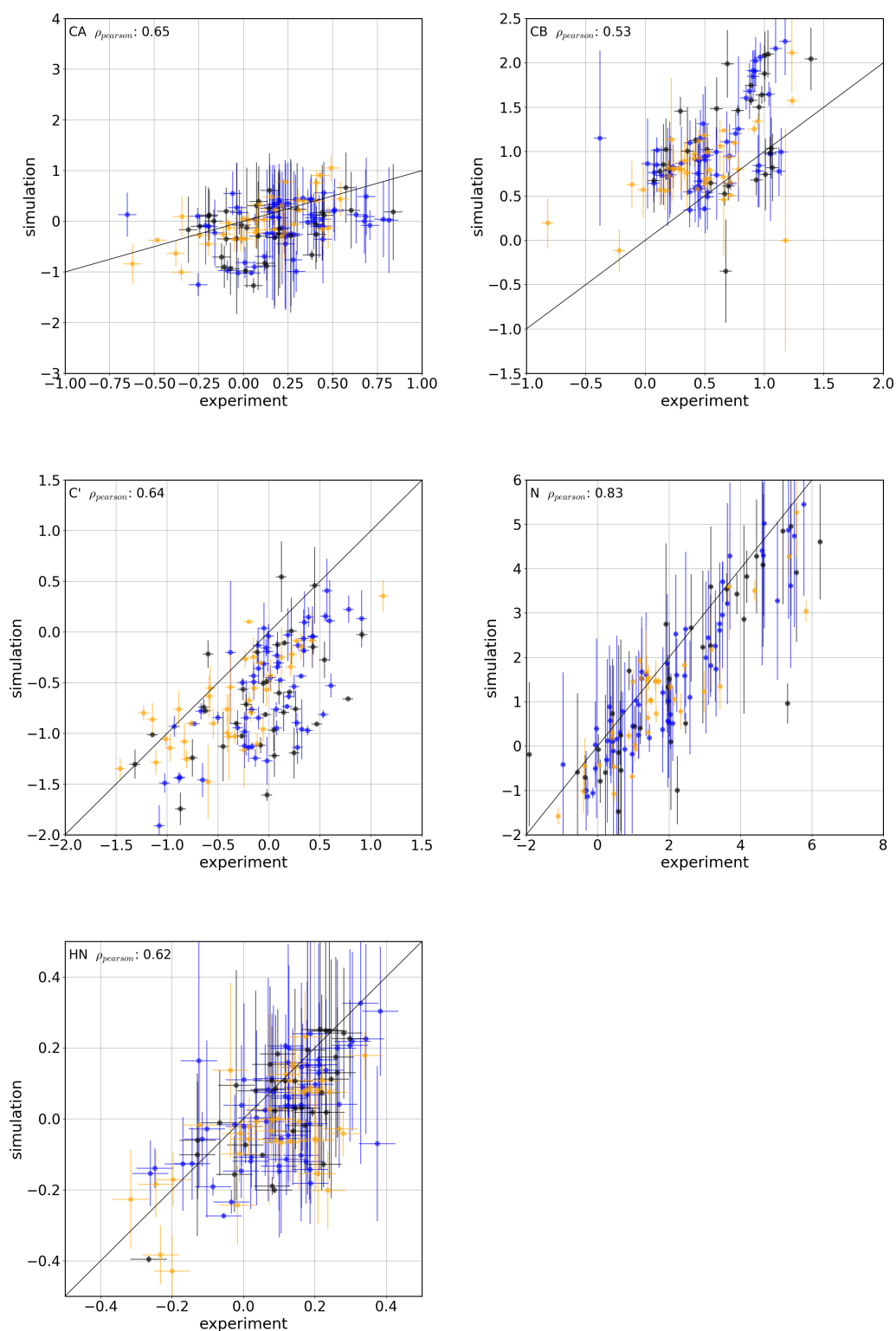**Error estimation of chemical shift calculations**

RMSDs were calculated between the raw chemical shifts measured in experiments (Mantsyzov et al. [57] and Schwalbe et al. [31]), those calculated from our AMBER03WS/TIP4P2005s MD structure ensemble and the model ensembles from Allison et al. [41] and Schwalbe et al. [31]. Chemical shifts were calculated with the programs SPARTA+ (SPP) and SHIFTX2 (SX2).
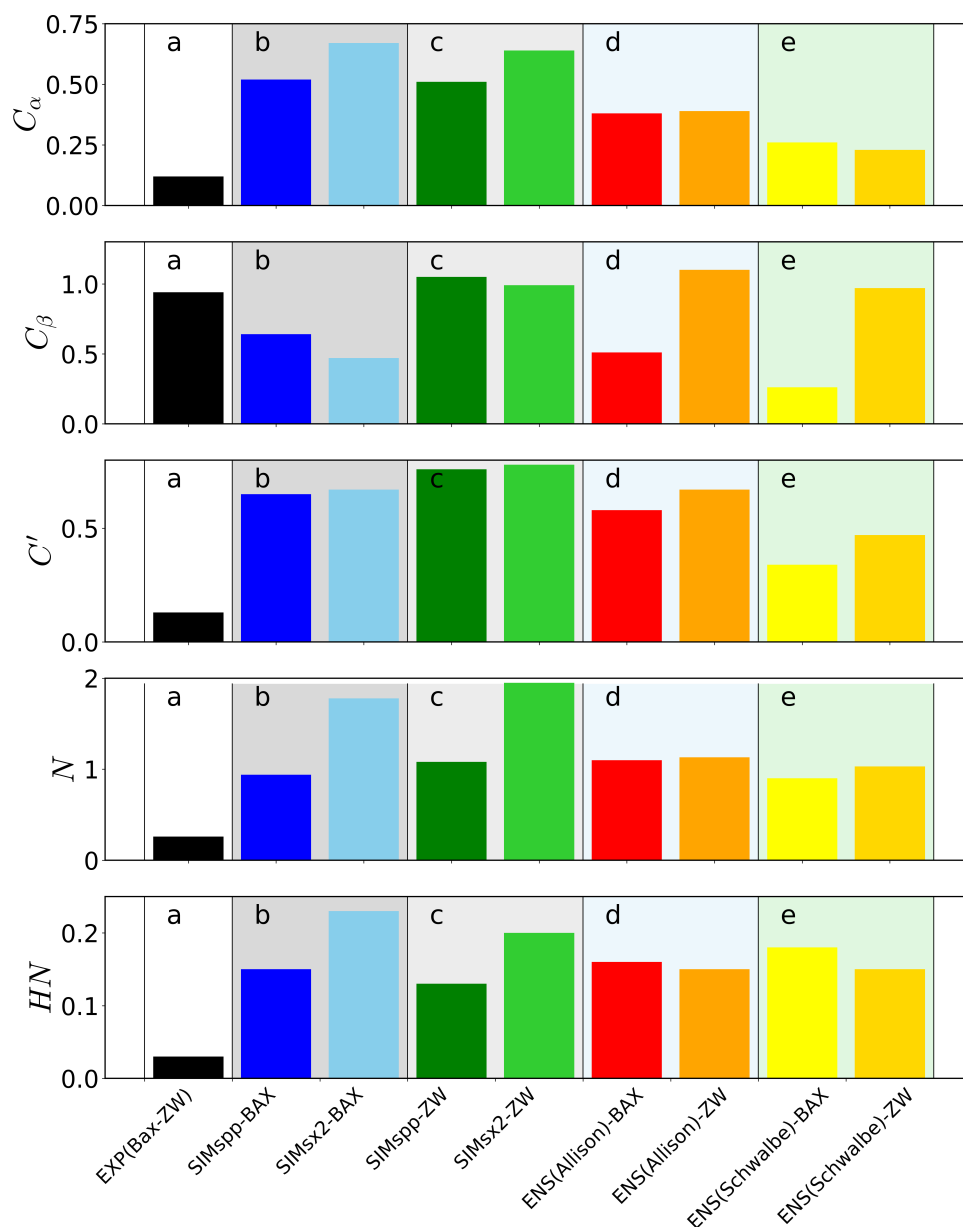

Fig S24. RMSD of chemical shifts (a): between experiments of Mantsyzov et al. [57](BAX) and Schwalbe et al. [31](ZW), (b): MD ensemble (either SPP or SX2) and BAX, (c): MD ensemble (either SPP or SX2) and ZW, (d): model ensemble Allison et al. [41](only SPP) and BAX (d): model ensemble Schwalbe et al.(only SPP) and ZW.

References

1. Hess B, Kutzner C, van der Spoel D, Lindahl E. GROMACS 4: Algorithms for Highly Efficient, Load-Balanced, and Scalable Molecular Simulation. Journal of Chemical Theory and Computation. 2008;4(3):435–447.

2. Hukushima K, Nemoto K. Exchange Monte Carlo method and application to spin glass simulations. Journal of the Physical Society of Japan. 1996;65(6):1604–1608.

3. Okabe T, Kawata M, Okamoto Y, Mikami M. Replica-exchange Monte Carlo method for the isobaric–isothermal ensemble. Chemical Physics Letters. 2001;335(5):435–439.

4. Seibert MM, Patriksson A, Hess B, Van Der Spoel D. Reproducible polypeptide folding and structure prediction using molecular dynamics simulations. Journal of Molecular Biology. 2005;354(1):173–183.

5. van der Spoel D, Seibert MM. Protein folding kinetics and thermodynamics from atomistic simulations. Physical Review Letters. 2006;96(23):238102.

6. Lei H, Duan Y. Improved sampling methods for molecular simulation. Current Opinion in Structural Biology. 2007;17(2):187–191.

7. Pan AC, Weinreich TM, Piana S, Shaw DE. Demonstrating an order-of-magnitude sampling enhancement in molecular dynamics simulations of complex protein systems. Journal of chemical theory and computation. 2016;12(3):1360–1367.

8. Bertoncini CW, Jung YS, Fernandez CO, Hoyer W, Griesinger C, Jovin TM, et al. Release of log-range tertiary interactions potentiates aggregation of natively unstructured α-synuclein. Proceedings of the National Academy of Sciences. 2005;102:1430–1435.

9. Joung IS, Cheatham III TE. Determination of alkali and halide monovalent ion parameters for use in explicitly solvated biomolecular simulations. The Journal of Physical Chemistry B. 2008;112(30):9020–9041.

10. Bussi G, Donadio D, Parrinello M. Canonical sampling through velocity rescaling. The Journal of Chemical Physics. 2007;126(1):014101.

11. Berendsen HJ, Postma Jv, van Gunsteren WF, DiNola A, Haak J. Molecular dynamics with coupling to an external bath. The Journal of Chemical Physics. 1984;81(8):3684–3690.

12. Essmann U, Perera L, Berkowitz ML, Darden T, Lee H, Pedersen LG. A smooth particle mesh Ewald method. The Journal of Chemical Physics. 1995;103(19):8577–8593.

13. Hess B, Bekker H, Berendsen HJ, Fraaije JG, et al. LINCS: a linear constraint solver for molecular simulations. Journal of Computational Chemistry. 1997;18(12):1463–1472.

14. Hess B. P-LINCS: A parallel linear constraint solver for molecular simulation. Journal of Chemical Theory and Computation. 2008;4(1):116–122.

15. Miyamoto S, Kollman PA. SETTLE: An analytical version of the SHAKE and RATTLE algorithms for rigid water models. Journal of Computational Chemistry. 1992;13:952–962.

16. Sezer D, Freed JH, Roux B. Parametrization, molecular dynamics simulation, and calculation of electron spin resonance spectra of a nitroxide spin label on a polyalanine α-helix. The Journal of Physical Chemistry B. 2008;112(18):5755–5767.

17. Ding F, Layten M, Simmerling C. Solution Structure of HIV-1 Protease Flaps Probed by Comparison of Molecular Dynamics Simulation Ensembles and EPR Experiments. Journal of the American Chemical Society. 2008;130(23):7184–7185.

18. Duan Y, Wu C, Chowdhury S, Lee MC, Xiong G, Zhang W, et al. A point-charge force field for molecular mechanics simulations of proteins based on condensed-phase quantum mechanical calculations. Journal of Computational Chemistry. 2003;24(16):1999–2012.

19. Best RB, Zheng W, Mittal J. Balanced Protein–Water Interactions Improve Properties of Disordered Proteins and Non-Specific Protein Association. Journal of Chemical Theory and Computation. 2014;10(11):5113–5124.

20. Abascal JL, Vega C. A general purpose model for the condensed phases of water: TIP4P/2005. The Journal of Chemical Physics. 2005;123(23):234505.

21. Piana S, Lindorff-Larsen K, Shaw DE. How robust are protein folding simulations with respect to force field parameterization? Biophysical Journal. 2011;100(9):L47–L49.

22. MacKerell Jr AD, Bashford D, Bellott M, Dunbrack Jr RL, Evanseck JD, Field MJ, et al. All-atom empirical potential for molecular modeling and dynamics studies of proteins†. The Journal of Physical Chemistry B. 1998;102(18):3586–3616.

23. MacKerell AD, Feig M, Brooks CL. Extending the treatment of backbone energetics in protein force fields: Limitations of gas-phase quantum mechanics in reproducing protein conformational distributions in molecular dynamics simulations. Journal of Computational Chemistry. 2004;25(11):1400–1415.

24. Piana S, Donchev AG, Robustelli P, Shaw DE. Water Dispersion Interactions Strongly Influence Simulated Structural Properties of Disordered Protein States. The Journal of Physical Chemistry B. 2015;119(16):5113–5123.

25. Hornak V, Abel R, Okur A, Strockbine B, Roitberg A, Simmerling C. Comparison of multiple Amber force fields and development of improved protein backbone parameters. Proteins: Structure, Function, and Bioinformatics. 2006;65(3):712–725.

26. Best RB, Hummer G. Optimized molecular dynamics force fields applied to the helix- coil transition of polypeptides. The Journal of Physical Chemistry B. 2009;113(26):9004–9015.

27. Lindorff-Larsen K, Piana S, Palmo K, Maragakis P, Klepeis JL, Dror RO, et al. Improved side-chain torsion potentials for the Amber ff99SB protein force field. Proteins: Structure, Function, and Bioinformatics. 2010;78(8):1950–1958.

28. Mahoney MW, Jorgensen WL. A five-site model for liquid water and the reproduction of the density anomaly by rigid, nonpolarizable potential functions. The Journal of Chemical Physics. 2000;112(20):8910–8922.

29. Grupi A, Haas E. Segmental Conformational Disorder and Dynamics in the Intrinsically Disordered Protein α-synuclein-Synuclein and Its Chain Length Dependence. Journal of Molecular Biology. 2011;405(5):1267–1283.

30. Grupi A, Haas E. Time-Resolved FRET Detection of Subtle Temperature-Induced Conformational Biases in Ensembles of α-Synuclein Molecules. Journal of Molecular Biology. 2011;411(1):234–247.

31. Schwalbe M, Ozenne V, Bibow S, Jaremko M, Jaremko L, Gajda M, et al. Predictive Atomic Resolution Descriptions of Intrinsically Disordered hTau40 and α-Synuclein in Solution from NMR and Small Angle Scattering. Structure. 2014;22(2):238–249.

32. Kumar S, Rosenberg JM, Bouzida D, Swendsen RH, Kollman PA. The weighted histogram analysis method for free-energy calculations on biomolecules. I. The method. Journal of Computational Chemistry. 1992;13(8):1011–1021.

33. Efron B, Tibshirani RJ. An introduction to the bootstrap. CRC press; 1994.

34. Morar AS, Olteanu A, Young GB, Pielak GJ. Solvent-induced collapse of α-synuclein and acid-denatured cytochrome c. Protein Science. 2001;10(11):2195–2199.

35. Wilkins DK, Grimshaw SB, Receveur V, Dobson CM, Jones JA, Smith LJ. Hydrodynamic radii of native and denatured proteins measured by pulse field gradient NMR techniques. Biochemistry. 1999;38(50):16424–16431.

36. Franke D, Petoukhov MV, Konarev PV, Panjkovich A, Tuukkanen A, Mertens HDT, et al. ATSAS 2.8: a comprehensive data analysis suite for small-angle scattering from macromolecular solutions. Journal of Applied Crystallography. 2017;50(4). doi:10.1107/S1600576717007786.

37. Schneidman-Duhovny D, Hammel M, Tainer JA, Sali A. Accurate SAXS profile computation and its assessment by contrast variation experiments. Biophysical Journal. 2013;105(4):962–974.

38. Schneidman-Duhovny D, Hammel M, Tainer JA, Sali A. FoXS, FoXSDock and MultiFoXS: Single-state and multi-state structural modeling of proteins and their complexes based on SAXS profiles. Nucleic Acids Research. 2016; p. gkw389.

39. Iwahara J, Schwieters CD, Clore GM. Ensemble approach for NMR structure refinement against 1H paramagnetic relaxation enhancement data arising from a flexible paramagnetic group attached to a macromolecule. Journal of the American Chemical Society. 2004;126(18):5879–5896.

40. Esteban-Martín S, Silvestre-Ryan J, Bertoncini CW, Salvatella X. Identification of fibril-like tertiary contacts in soluble monomeric α-synuclein. Biophysical Journal. 2013;105(5):1192–1198.

41. Allison JR, Varnai P, Dobson CM, Vendruscolo M. Determination of the Free Energy Landscape of α-Synuclein Using Spin Label Nuclear Magnetic Resonance Measurements. Journal of the American Chemical Society. 2009;131(51):18314–18326.

42. Hoefling M, Lima N, Haenni D, Seidel CAM, Schuler B, Grubmüller H. Structural Heterogeneity and Quantitative FRET Efficiency Distributions of Polyprolines through a Hybrid Atomistic Simulation and Monte Carlo Approach. PLoS ONE. 2011;6(5):e19791.

43. Best R, Hofmann H, Nettels D, Schuler B. Quantitative Interpretation of FRET Experiments via Molecular Simulation: Force Field and Validation. Biophysical Journal. 2015;108(11):2721–2731.

44. Schröder GF, Alexiev U, Grubmüller H. Simulation of Fluorescence Anisotropy Experiments: Probing Protein Dynamics. Biophysical Journal. 2005;89(6):3757–3770.

45. Steinhoff HJ, Karim C. Protein dynamics and EPR-spectroscopy: comparison of molecular dynamic simulations with experiments. Berichte der Bunsengesellschaft für Physikalische Chemie. 1993;97:163–163.

46. Hoefling M, Grubmüller H. In silico FRET from simulated dye dynamics. Computer Physics Communications. 2013;184(3):841–852.

47. Dexter DL. A theory of sensitized luminescence in solids. The Journal of Chemical Physics. 1953;21(5):836–850.

48. Kabsch W, Sander C. Dictionary of protein secondary structure: pattern recognition of hydrogen-bonded and geometrical features. Biopolymers. 1983;22(12):2577–2637.

49. Joosten RP, Te Beek TA, Krieger E, Hekkelman ML, Hooft RW, Schneider R, et al. A series of PDB related databases for everyday needs. Nucleic Acids Research. 2011;39(suppl 1):D411–D419.

50. Ensign DL, Pande VS. Bayesian single-exponential kinetics in single-molecule experiments and simulations. The Journal of Physical Chemistry B. 2009;113(36):12410–12423.

51. Schröder GF, Grubmüller H. Maximum likelihood trajectories from single molecule fluorescence resonance energy transfer experiments. The Journal of Chemical Physics. 2003;119(18):9920–9924.

52. Svergun D, Barberato C, Koch MHJ. CRYSOL–a program to evaluate X-ray solution scattering of biological macromolecules from atomic coordinates. Journal of applied crystallography. 1995;28(6):768–773.

53. Chen Pc, Hub JS. Interpretation of Solution X-Ray Scattering by Explicit-Solvent Molecular Dynamics. Biophysical Journal. 2015;108(10):2573–2584.

54. Ulmer TS, Bax A, Cole NB, Nussbaum RL. Structure and dynamics of micelle-bound human α-synuclein. Journal of Biological Chemistry. 2005;280(10):9595–9603.

55. Uversky VN, Li J, Fink L. Evidence for a Partially Folded Intermediate in α-Synuclein Fibril Formation. Journal of Biological Chemistry. 2001;276(14):10737–10744.

56. Rekas A, Knott RB, Sokolova A, Barnham KJ, Perez KA, Masters CL, et al. The structure of dopamine induced α-synuclein oligomers. European Biophysics Journal. 2010;39(10):1407–1419.

57. Mantsyzov AB, Maltsev AS, Ying J, Shen Y, Hummer G, Bax A. A maximum entropy approach to the study of residue-specific backbone angle distributions in α-synuclein, an intrinsically disordered protein. Protein Science. 2014;23(9):1275–1290.

58. Vuister GW, Delaglio F, Bax A. The use of $1J_{C\alpha H\alpha}$ coupling constants as a probe for protein backbone conformation. Journal of Biomolecular NMR. 1993;3(1):67–80.

59. Gapsys V, Narayanan RL, Xiang S, de Groot BL, Zweckstetter M. Improved validation of IDP ensembles by one-bond Cα–Hα scalar couplings. Journal of biomolecular NMR. 2015;63(3):299–307.

60. Wirmer J, Schwalbe H. Angular dependence of $^1J(N_i, C\alpha_i)$ and $^2J(N_i, C\alpha_{i-1})$ coupling constants measured in J-modulated HSQCs. Journal of Biomolecular NMR. 2002;23(1):47–55.

61. Vuister GW, Bax AD. Quantitative J correlation: a new approach for measuring homonuclear three-bond $J(H^N H^\alpha)$ coupling constants in ^{15}N-enriched proteins. Journal of the American Chemical Society. 1993;115(17):7772–7777.

62. Vögeli B, Ying J, Grishaev A, Bax A. Limits on Variations in Protein Backbone Dynamics from Precise Measurements of Scalar Couplings. Journal of the American Chemical Society. 2007;129(30):9377–9385.

63. Peter C, Daura X, Van Gunsteren WF. Calculation of NMR-relaxation parameters for flexible molecules from molecular dynamics simulations. Journal of Biomolecular NMR. 2001;20:297–310.

64. Han B, Liu Y, Ginzinger SW, Wishart DS. SHIFTX2: significantly improved protein chemical shift prediction. Journal of biomolecular NMR. 2011;50(1):43–57.

65. Kjaergaard M, Brander S, Poulsen FM. Random coil chemical shift for intrinsically disordered proteins: effects of temperature and pH. Journal of Biomolecular NMR. 2011;49(2):139–149.

66. Kjaergaard M, Poulsen FM. Sequence correction of random coil chemical shifts: correlation between neighbor correction factors and changes in the Ramachandran distribution. Journal of Biomolecular NMR. 2011;50(2):157–165.